ACCSCIENCE PUBLISHING

International Journal of Bioprinting

ACCEPTED PAPER · MAIN TEXT

Suspended 3D printing of polycaprolactone/hydroxyapatite composites for mimicking complex structured bone scaffolds

Article ID: IJB025320319

Citation: Kang J, Shirzad M, Ranganathan P, *et al*. Suspended 3D printing of polycaprolactone/hydroxyapatite composites for mimicking complex structured bone scaffolds. *Int J Bioprint*. doi: 10.36922/IJB025320319

AccScience Publishing

RESEARCH ARTICLE

Volume X Issue X (2025)

doi: 10.36922/IJB025320319

Suspended 3D printing of polycaprolactone/hydroxyapatite composites for mimicking complex structured bone scaffolds

Running title: Suspended 3D printing of PCL/HA composites

Juhyun Kang[1†], Masoud Shirzad[2†], Priya Ranganathan[2], Dageon Oh[2], Sudip Mondal[3], Junghwan Oh[1, 2, 5], Hae Gyun Lim[1, 2, 4], Mahdi Bodaghi[5*], and Seung Yun Nam[1, 2, 4*]

[1] Department of Biomedical Engineering, Pukyong National University, Busan 48513, Republic of Korea

[2] Industry 4.0 Convergence Bionics Engineering, Pukyong National University, Busan 48513, Republic of Korea

[3] Digital Healthcare Research Center, Pukyong National University, Busan 48513, Republic of Korea

[4] Major of Biomedical Engineering, Division of Smart Healthcare, College of Information Technology and Convergence, Pukyong National University, Busan 48513, Republic of Korea

[5] Department of Engineering, School of Science and Technology, Nottingham Trent University, Nottingham NG11 8NS, UK

†*These authors contributed equally to this work.*

***Corresponding authors:**

Seung Yun Nam(synam@pknu.ac.kr)

Mahdi Bodaghi (mahdi.bodaghi@ntu.ac.uk)

Citation: Kang J, Shirzad M, Ranganathan P, *et al.* Suspended 3D printing of polycaprolactone/hydroxyapatite composites for mimicking complex structured bone scaffolds. *Int J Bioprint*. doi: 10.36922/IJB025320319

Received: August 8, 2025

1st revised: August 25, 2025

2nd revised: August 29, 2025

Accepted: September 1, 2025

Published Online: September 2, 2025

Abstract

Extrusion-based 3D printing has been rapidly advancing as a key technique for fabricating tissue engineering scaffolds. However, 3D printing complex structures with appropriate mechanical strength and biocompatibility remains a challenge. Suspended 3D printing is an emerging fabrication strategy that enables the creation of tissues or organs by a support medium that provides a stable printing environment without the need for additional support structures. This study presents a novel strategy for fabricating intricate scaffolds using suspended 3D printing of bioinks incorporating dissolved PCL (dPCL) and hydroxyapatite (HA). The optimized dPCL/HA bioink demonstrated up to an 85% reduction of print errors compared to conventional methods, significantly improving 3D printability. Moreover, mechanical assessments revealed a compressive Young's modulus approximately 50 MPa higher in dPCL/HA scaffolds than dPCL scaffolds. Furthermore, dPCL/HA scaffolds outperformed both PCL and dPCL scaffolds in cell proliferation tests. Complex 3D shapes, including helices, saddles, multi-curvature structures, hollow hemispheres, and zygomatic bones, were successfully 3D printed, demonstrating the ability to mimic natural and intricate anatomical structures of the human body. These approaches pave the way for 3D printing patient-specific and structurally robust bone constructs with enhanced mechanical and biological properties.

Keywords: Extrusion-based 3D printing; Suspended 3D printing; Bone tissue engineering; Biomimetic scaffolds; Composites

1. Introduction

Complex bone defects resulting from fractures, osteoporosis, and infections pose significant challenges to the healing process due to the intricate biomechanical and biological demands of bone tissues [1-3]. Addressing these critical requirements demands advanced strategies to accelerate the healing process. The implementation of biocompatible scaffolds represents one such strategy, offering appropriate mechanical and biological properties to support the growth of host tissues [4]. Over the past few years, a variety of conventional and advanced strategies have been developed for the fabrication of tissue engineering scaffolds. Among these methods, extrusion-based three-dimensional (3D) printing has emerged as a promising approach, enabling the construction of scaffolds through the repetitive, layer-by-layer deposition of biomaterials while offering a wide range of material choices [5-7]. However, conventional extrusion-based printing methods face significant limitations, particularly in fabricating complex 3D geometries. These structures often require additional support structures, making the process time-consuming and less efficient [8,9].

To overcome these limitations, suspended 3D printing was introduced as an advanced technique, enhancing extrusion-based 3D printing by allowing the fabrication of detailed structures without the need for additional construction of supports [10-12]. This method utilizes a support medium, such as a gel or viscous liquid, to facilitate freeform construction in multiple directions, allowing the creation of complex structures. Moreover, compared to conventional extrusion-based 3D printing, suspended 3D printing offers greater flexibility in material selection, which is particularly advantageous for fabricating functional tissue-engineered constructs [13-15]. This method promotes the formation of perfusable vascular channels and supports the integration of native tissue components by maintaining the spatial fidelity of soft hydrogels. Despite these advancements, the application of suspended 3D printing in bone tissue engineering remains limited, primarily due to the insufficient mechanical properties of conventional hydrogel-based bioinks, which are often inadequate for load-bearing environments [16,17]. More importantly, most studies that have employed the room-temperature suspended printing method have predominantly focused on hydrogel inks rather than thermoplastic polymers [14,15].

In the fabrication of the bone scaffolds, polycaprolactone (PCL) has been widely used due to its excellent biocompatibility and favorable mechanical properties. In addition, combining PCL with hydroxyapatite (HA), which constitutes approximately 70% of bone composition, has also been extensively studied because HA enhances the biofunctionality and compressive modulus of bone scaffolds [18-22]. However, PCL, which is generally printed at 60ºC or higher, is limited to suspended printing in gel with high moisture content at room temperature [23]. Notably, one previous study attempted the melt-printing of PCL within a thermally stable support matrix. However, this approach required printing at elevated temperatures over 65ºC, limiting its applicability to biologically or thermally sensitive conditions [24].

To address these challenges, this study aims to overcome the limitations associated with conventional 3D printing methods for fabricating complex bone scaffolds by utilizing suspended 3D printing with PCL/HA composites at room temperature. Based on this, the physicochemical properties of the dissolved-PCL (dPCL) integrated with HA were quantitatively evaluated by Fourier-transform infrared spectroscopy (FTIR), X-ray diffraction (XRD), thermogravimetric analysis (TGA), contact angle analysis, scanning electron microscopy (SEM), and field emission scanning electron microscopy (FE-SEM). Additionally, the printability and rheological properties of the suspended 3D printing process were quantitatively analyzed. Moreover, the rheological properties were assessed for both the polymer and composites. Mechanical properties were also evaluated under tensile and compressive loads, and cell proliferation tests were conducted to assess the biological effects of the present strategy using the alamarBlue assay. A schematic overview of the study design is provided in Figure 1. Furthermore, a comparative summary between the present study and previously published papers is provided to highlight the novelty of this work and demonstrate its advantages over prior studies (Table 1).

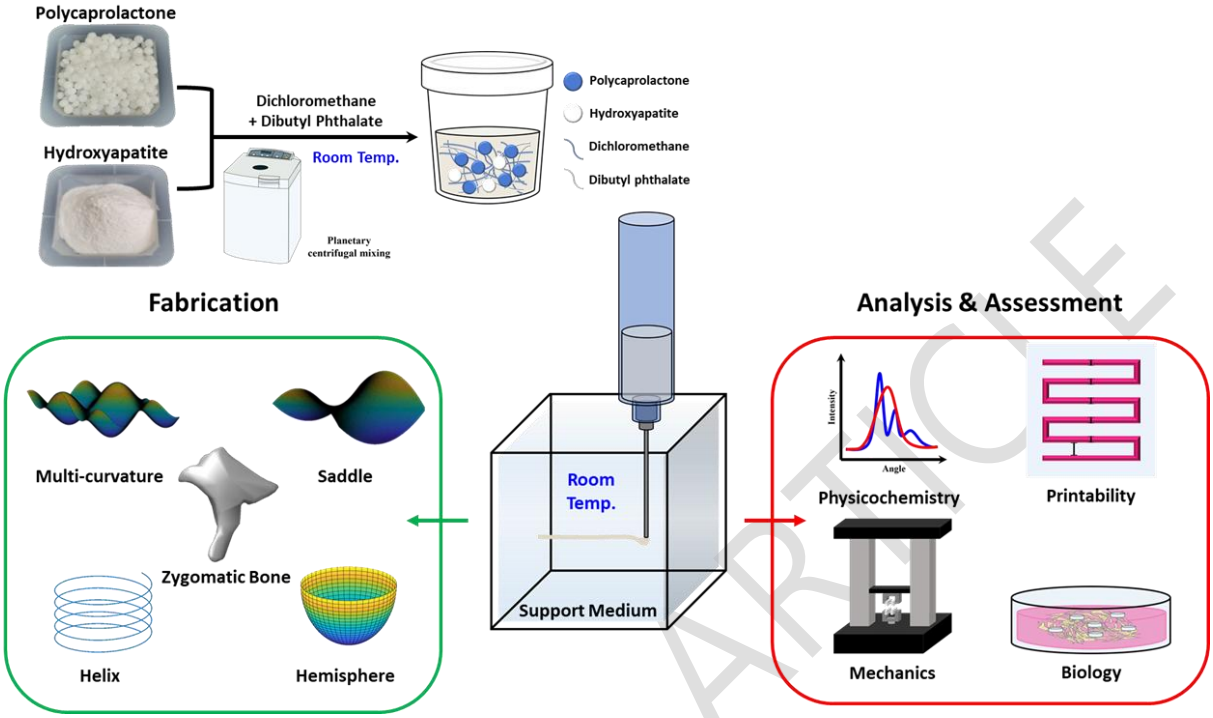

Figure 1. Schematic illustration of the suspended 3D printing process for fabricating complex structures using dPCL/HA composites.

Table 1. Comparison of different printing methods with the present study for the fabrication of bone scaffolds.

Method	Temperature	High viscosity/ mechanical properties	Support printing	Complexity of post processing	Reference
Suspended	Low	Available	Available	Low	Current Study
Suspended	Moderate	N/A	Available	Low	[3], [6], [10 - 15], [24], [40], [41], [52]
Conventional	High	Variable	N/A	High	[4], [5], [7], [8], [20], [25], [30], [34], [35], [39], [42], [44], [45], [49], [50], [51], [53], [55], [56], [57]
Photo-polymerization	Low	Available	N/A	High	[8], [43]

2. Materials and Methods

2.1. Hydroxyapatite Synthesis

Hydroxyapatite (HA) powder was synthesized via a wet precipitation method using calcium nitrate tetrahydrate ($Ca(NO_3)_2{\cdot}4H_2O$, Sigma Aldrich) and di-ammonium hydrogen phosphate ($(NH_4)_2HPO_4$, Supelco). In this method, ammonium hydroxide solution (NH_4OH (28-30%), Sigma Aldrich) was used as a precipitating agent. A 0.24 M solution of $Ca(NO_3)_2{\cdot}4H_2O$ was stirred vigorously at room temperature. Subsequently, a 0.29 M solution of $(NH_4)_2HPO_4$ was slowly added to the $Ca(NO_3)_2{\cdot}4H_2O$ solution. The pH of the final mixture was adjusted to 11 by adding

an ammonium hydroxide solution. After a reaction period of 6 hours and an aging period of over 12 hours, the precipitate was filtered out of the reaction solution until a neutral pH was reached. The filtered precipitate was dried overnight at 90ºC. The dried precipitate was calcined at 600°C for 1 h in air to remove residual volatiles and ensure crystallinity of the apatite phase prior to compounding [18].

2.2. Bioink & Support Medium Preparation

This research aimed to prepare a suspended bioink using two solvents to dissolve polycaprolactone (PCL, Mw: 50,000; Polysciences) and hydroxyapatite (HA), enabling their printability at room temperature. Dichloromethane (DCM, evaporator, Sigma Aldrich) and dibutyl phthalate (DBP, plasticizer, Sigma Aldrich) were mixed in a 10:1 (v/v) ratio based on the total weight of PCL and HA at room temperature. PCL was subsequently dissolved in the mixed solvent to produce dissolved PCL (dPCL). dPCL/HA refers to a mixture of dPCL and HA in a 7:3 ratio (w/w), respectively. Both components were homogeneously blended using a planetary centrifugal mixer (AR-100, THINKY Corporation). It is worth noting that PCL scaffolds were fabricated using a customized extrusion-based printer at 120ºC. Laponite-based support medium (BYK) at various concentrations was prepared by homogeneous mixing in distilled water using a magnetic stirrer at 500 rpm for 10 minutes. Subsequently, the mixture was transferred to a cubic-shaped container ($40 \times 40 \times 40$ mm^3) and allowed to gel over 24 hours at room temperature.

2.3. Physicochemical Analysis

Fourier-transform infrared spectroscopy (FTIR) was conducted using the FTIR instrument (FT-4100, JASCO) in the scan range of 4000-650 cm^{-1}. X-ray diffraction analysis (XRD, Ultima IV, Rigaku) utilized Cu Kα radiation (λ=1.5406 Å) at 40 kV and 30 mA. The diffraction angles (2θ) were scanned with a step size of 0.02° 2θ per second in the scan range of 10 - 70°. The HA powder

and fabricated scaffolds were compared to the HA standard diffraction data (JCPDS# 72-1243). Thermogravimetry analysis (TGA, Discovery TGA 55, TA Instruments) was performed in N_2 with a heating rate of 10ºC/min and an end temperature of 700ºC. Contact angle analysis was assessed via a contact angle analyzer (Phoenix MT, SEO). Morphological analysis was conducted with the field emission scanning electron microscope (FE-SEM, MIRA3, Tescan, 15kV) and the scanning electron microscope (SEM, Vega2, Tescan, 10kV). Furthermore, a comparison of surface roughness (Ra) and structural shape scanning was performed by a 3D optical profiler (VR-5200, Keyence) that scans optics vertically on a measurement platform.

2.4. Printability Assessment

The rheological properties of the PCL/HA composites were assessed employing a rheometer (HR-2, TA Instruments) with a 20 mm parallel plate and a 1000 μm gap. A solvent trap was used in all assessments to prevent drying. The frequency sweep test for bioink was performed by varying the angular frequency from 0.1 to 100 rad/s at 25ºC with 0.1% strain. The recovery test of the support medium involved three steps. The initial and third steps were performed at a shear rate of 0.1/s for 60 seconds, and the second step was conducted at a shear rate of 100/s for 10 seconds. All steps were performed under 25ºC. Additionally, the following printing parameters were used: a pressure of 450 kPa and a 21-gauge (0.52 mm) nozzle. These parameters were applied to assess three factors in two different printing directions: vertical thickness (side), axial position error (side), and horizontal thickness (bottom) across varying nozzle speeds ranging from 1 to 6 mm/s (Figure 3(A)).

To measure the thickness of the printed strands, a MATLAB code was implemented to calculate the number of pixels, which was then multiplied by the pixel resolution and converted into millimeters. Any single-line section of the strand that did not match the expected color was excluded to minimize potential errors. Subsequently, mean and standard deviation values were calculated from these assessments.

This research focused on the central section to assess the printed strand thickness. The strand step was set to 2 mm for thickness measurement. Thickness was evaluated by applying the following relationship:

$$Strand\ thickness\ (mm) = \frac{\sum(P_N \times P_R)}{N} \quad (\text{I})$$

Where P_N is the counted pixel per line, P_R is the calculated resolution of pixel per millimeter, and N is the total number of counted pixels.

The repeated layering was printed after the standard strand with a 2 mm step to assess axial position error. Axial position error was evaluated by using the following relationship:

$$Axial\ position\ error\ (\%) = \frac{H_O - H_D}{H_O} \times 100 \quad (\text{II})$$

Where H_O denotes the original height of the feature and H_D is the deformed height of the feature.

2.5. Mechanical Assessment

The mechanical properties of conventionally and suspended 3D-printed scaffolds were evaluated via a universal testing machine (LR5K Plus, LLOYD Instruments). Compressive specimens were prepared as 5 × 5 × 5 mm^3 cubes, and tensile specimens were fabricated from 0.5 × 5 × 30 mm^3 plates. All the compression and tensile tests were conducted at a constant crosshead speed.

2.6. Biological Analysis

The scaffolds were fabricated as sheets and then punched with a 5 mm biopsy punch. After sterilization with 70 % ethanol and phosphate-buffered saline (PBS) over 7 days, the scaffolds were incubated in Dulbecco's modified Eagle's medium (DMEM) at 37ºC in a humidified atmosphere of 5% CO_2 for 24 hours before cell seeding. Rat adipose-derived mesenchymal stem cells (rADSCs, Cyagen) at passage 5 were seeded onto scaffolds at a density of 2.0×10^5 cells per scaffold. The cells were then cultured in DMEM supplemented with 10% fetal bovine serum (FBS)

and 1% penicillin-streptomycin at 37ºC with 5% CO_2. After one day of cultivation, cell proliferation was determined using alamarBlue reagents (alamarBlue™, Invitrogen) by incubating the scaffolds for 4 hours with 10 % alamarBlue reagent at 37ºC. The alamarBlue assay was quantified using a UV-Vis spectrophotometer (Epoch, BioTek) at 570 nm and 600 nm absorbance.

3. Results and Discussion

A comprehensive physicochemical analysis was performed to verify the effective preservation of the chemical and structural properties of PCL and HA, confirming stable synthesis and efficient mixing of the materials. Figure 2(A) displays the FTIR spectra of the HA, PCL, and PCL-based composites. The synthesized HA exhibited characteristic peaks at 962, 1024, and 1088 cm^{-1}, which were attributed to P-O bending vibrations, in addition to a peak at 3573 cm^{-1}, corresponding to O-H stretching from the hydroxyl group. The spectra of PCL and dPCL showed peaks at 1164 and 1238 cm^{-1} for C-O-C, 1721 cm^{-1} for C=O stretching of ester groups, and 2866 and 2942 cm^{-1} for C-H stretching. Notably, the spectra of dPCL closely resembled those of PCL, indicating that the dissolution and processing of PCL did not considerably alter its chemical structure. In the dPCL/HA composite, a decrease in transmittance was observed for C=O and C-H bonds compared to their respective values in pure PCL and HA. However, the retention of the majority of the characteristic peaks from both PCL and HA confirmed that the original chemical properties of these materials were preserved throughout the synthesis and mixing process. This finding demonstrates the successful integration of HA into the PCL without significant chemical degradation.

The XRD analysis of PCL, HA, and dPCL/HA provided insights into their crystalline structure (Figure 2(B)). The dPCL displayed characteristic peaks at 2θ values of 21.5° and 23.8°, corresponding to the crystalline structure of PCL. These peaks were also prominent in the dPCL/HA composite, indicating the incorporation of HA did not disrupt the crystalline structure of PCL. The HA peaks, obtained at 2θ of 25.87º, 31.74º and 32.86º, matched the reference data for JCPDS 72-1243. In the dPCL/HA composite, weaker HA peaks were observed, indicating partial

crystallization of HA within the composite. Importantly, despite this partial crystallization, the primary crystalline characteristics of PCL were preserved, as confirmed by the consistent peaks.

As illustrated in Figure 2(G), the TGA analysis was conducted to assess the thermal stability of the composite. HA demonstrated great thermal stability up to 700°C. In contrast, both dPCL and dPCL/HA displayed a significant weight loss, beginning at approximately 400°C, corresponding to the thermal decomposition of PCL. Interestingly, the dPCL/HA retained approximately 30% of residual weight at elevated temperatures, attributed to the incorporation of non-combustible HA embedded within the composite. Furthermore, this value agrees with the intended 7:3 (w/w) composition and thus serves as an indirect indicator of batch-level compositional uniformity. Although the thermal degradation rates of both dPCL and dPCL/HA were slightly accelerated compared to pure PCL, the observed difference remained within acceptable limits, indicating that the composite materials possessed adequate thermal stability for practical applications. This stability was essential for ensuring adequate material properties in bone tissue engineering applications.

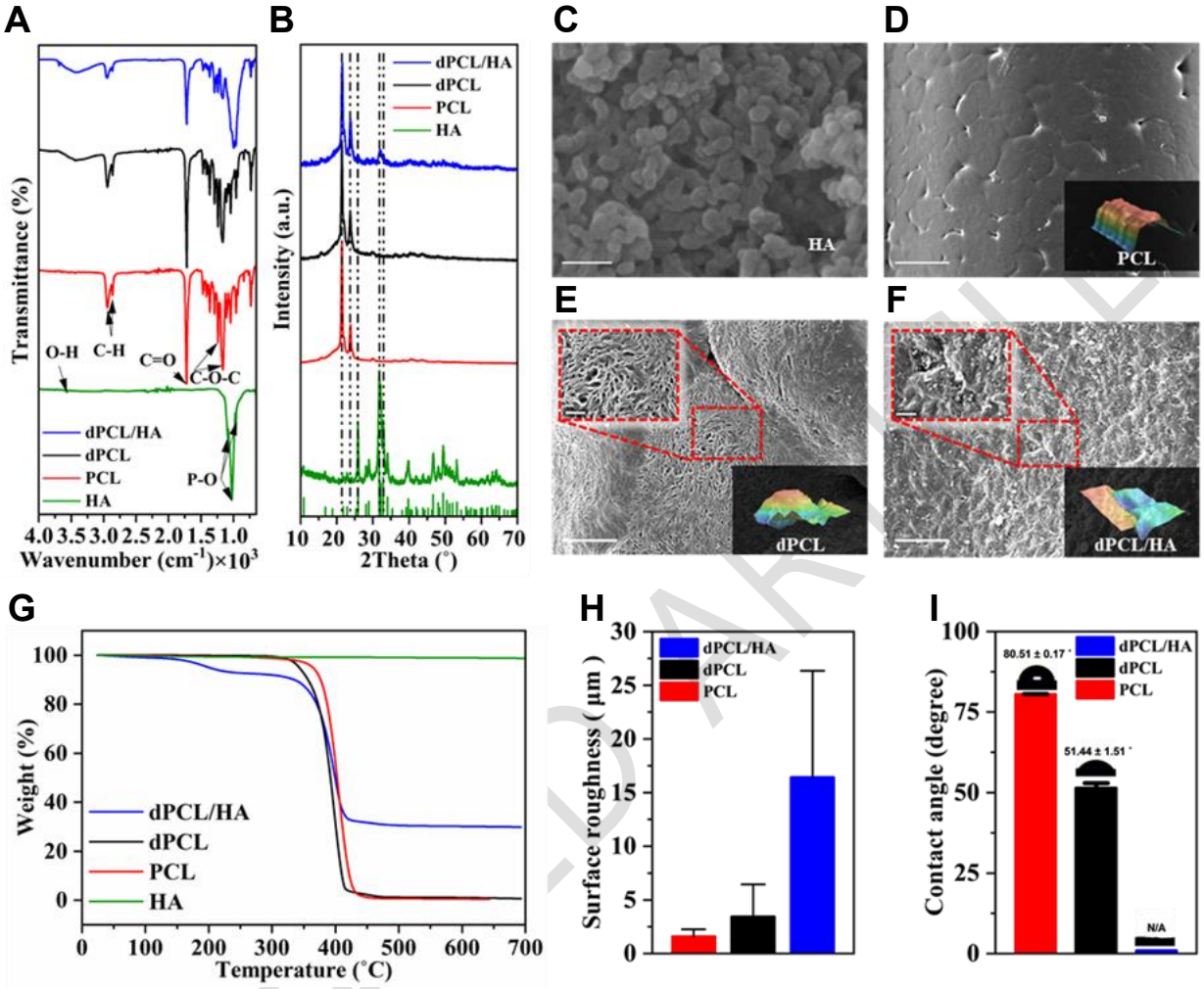

Figure 2. (A) FTIR spectra and (B) XRD patterns of PCL, dPCL, HA, and dPCL/HA. (C) FE-SEM image of HA particles (scale bar = 100 nm). SEM images of (D) PCL, (E) dPCL, and (F) dPCL/HA (scale bar = 50 μm in D-F; insets in E and F = 10 μm). (G) TGA curves, (H) surface roughness profiles (Ra), and (I) contact angle values of PCL, dPCL, and dPCL/HA scaffolds.

The HA particles were synthesized by the wet method, with a size of approximately 50 nm (Figure 2(C)). Figure 2(D) and 2(E) present SEM images of PCL and dPCL, respectively. Although inter-pore connectivity is not clearly visible in the image, micropores are distributed across the dPCL surface (Figure 2E). It is noteworthy that these micropores were not observed in pure PCL, suggesting that solvent evaporation induced surface porosity in dPCL. The microstructures found in these samples demonstrated similarities to the morphological properties of specimens prepared

via a gas foaming process [25]. These observations supported the assumption that the microporous structure in dPCL formed as a direct result of DCM volatilization. However, in Figure 2(F), dPCL/HA shows no pattern similar to dPCL, instead showing irregular topography with HA particles and crater-like features. These observations confirmed that HA could fill the space created by DCM.

As depicted in Figure 2(H), dPCL/HA (16.4 ± 9.9 μm) revealed significantly higher surface roughness compared to dPCL (3.4 ± 3 μm) and PCL (1.6 ± 0.7 μm). This increased surface roughness can provide a more suitable biocompatible environment. Interestingly, a notable difference in contact angle was observed (Figure 2(I)) between dPCL (51.44 ± 1.51 º) and PCL (80.51 ± 0.17 º). The exact contact angle for dPCL/HA could not be accurately measured, as water was fully absorbed at the initial stage of the assessment, possibly due to the vaporization of DCM and the strong hydrophilic properties of HA [26,27]. Consequently, the microporosity induced by DCM in dPCL significantly improved surface roughness and decreased the contact angle, while the HA integration further enhanced these properties. These modifications are critically beneficial in enhancing the bioactivity of the composite material, as both increased surface roughness and hydrophilicity strongly correlate with improved cellular attachment and tissue integration[28]. This study suggests that the dPCL/HA composite possesses favorable physicochemical and surface properties, making it highly promising in biomaterial applications, particularly in contexts where enhanced biocompatibility and cell-material interactions are essential. These enhancements significantly improve the potential applications of dPCL/HA composites as biomaterials [29,30].

Moreover, the rheological properties of the prepared dPCL and dPCL/HA were assessed using a frequency sweep test. As shown in Figure 3(B) and 3(C), the PCL-based ink demonstrated remarkable viscosity consistency. Both the storage modulus (G') and the loss modulus (G") showed a consistent, nearly linear increase with angular frequency ranging from 0.1 to 100 rad/s. However, the crossover phenomenon, typically defined as the point where G' and G" intersect in hydrogel-based inks, did not occur [31,32]. The absence of a crossover point indicates that the solid-like viscoelastic behavior of dPCL maintains stable rheological properties even as the frequency increases [33-35].

The complex viscosity of both dPCL and dPCL/HA inks was consistently maintained at approximately 190 Pa·s across the entire frequency range (0.1 to 100 rad/s). This stable viscosity facilitated uniform extrusion flow under varying shear conditions, making it particularly suitable for suspended 3D printing. Consequently, PCL-based inks exhibited stable elastic behavior even at elevated frequencies, indicating minimal changes in network structure. These unique rheological properties render dPCL and dPCL/HA inks particularly advantageous compared to hydrogel-based inks, which frequently experience lower viscosity and structural stability at higher shear rates [33,36].

Laponite RD-based support medium provides a stable suspended 3D printing environment for dPCL and dPCL/HA inks. Thixotropic behavior, defined as a reversible decrease in viscosity under applied stress followed by recovery upon stress removal, is a key factor influencing the recovery performance of Laponite RD. This recovery behavior strongly depends on both the strength of the particle network structure and the concentration of Laponite RD (Figure 3D) [37]. At concentrations of 3% and 4%, a noticeable gap was observed between the pre- and post-stress viscosities, indicating incomplete recovery due to insufficient network density. In contrast, the 5% and 6% concentrations exhibited nearly identical pre- and post-stress viscosities, reflecting a denser particle network that facilitates faster recovery. However, this rapid recovery can hinder strand formation, as the support medium stabilizes quickly and prevents sufficient spreading of the extruded bioink to fill cracks or voids generated by nozzle movement [15].

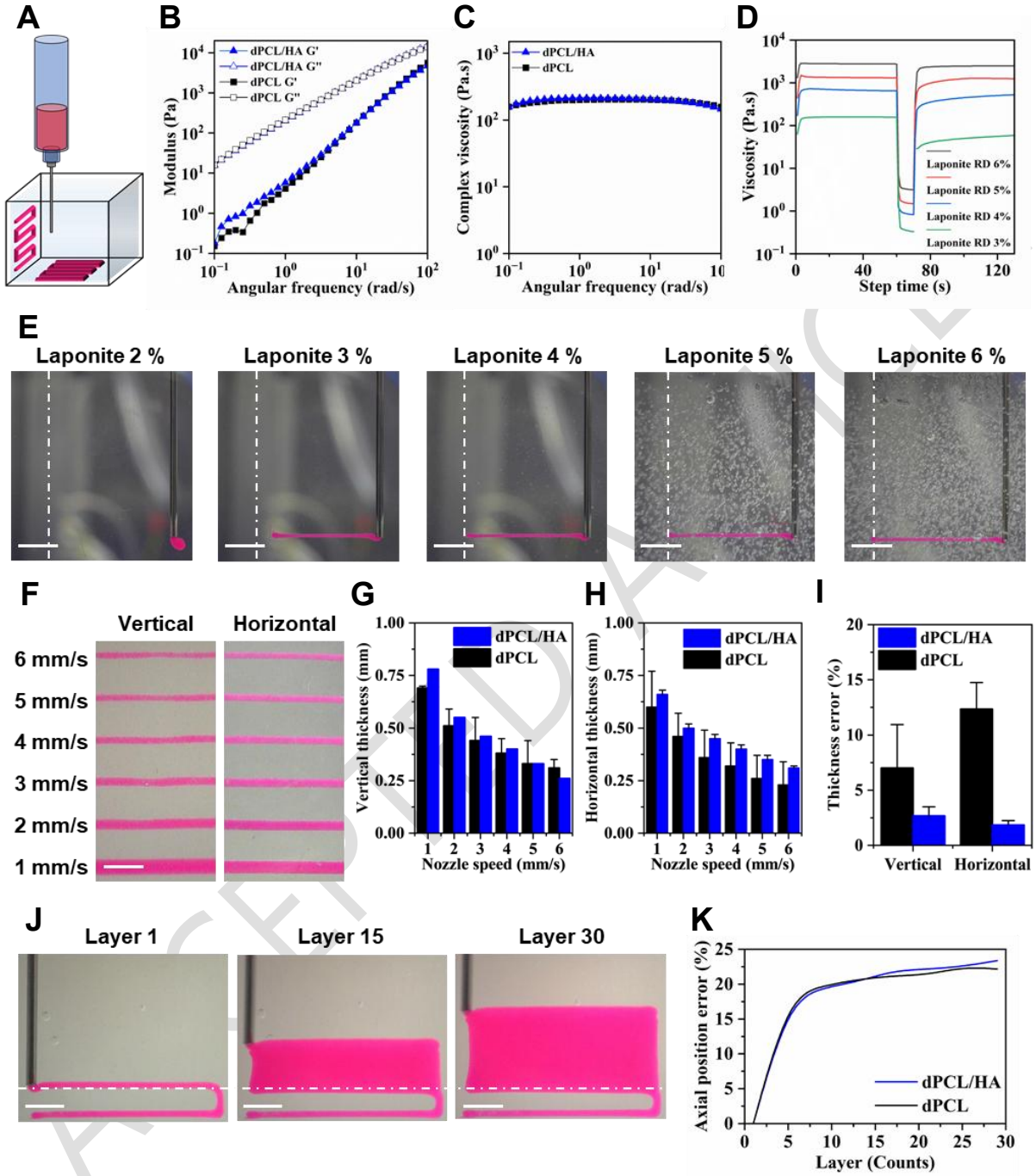

Figure 3. (A) Schematic illustration of printability assessment. (B) Storage modulus (G'), loss modulus (G"), and (C) complex viscosity of dPCL and dPCL/HA in frequency sweep tests. (D) Flow peak-hold test of the support media with various concentrations. (E) Printing test of the support media (scale bar = 5 mm). (F) Strand thickness tests under various nozzle speeds (scale bar = 2 mm). Strand thickness assessments for (G) vertical and (H) horizontal directions, and (I) strand thickness errors for both directions. (J) Images of axial position error tests (scale bar = 2 mm), and (K) the numerical evaluation of error rate with increasing layers.

In the next step, the fixation and stability of printed strands were evaluated at various concentrations of the support medium (Figure 3(E)). The results demonstrated that strands printed in 3-6% Laponite solutions remained fixed, while the 2% concentration yielded unstable shapes, forming irregular bioink bumps rather than defined structures. Although 5% and 6% concentrations provided sufficient fixation, the support medium entrapped bubbles and exhibited crevices during the printing process. These structural instabilities compromised print quality by affecting the medium's uniformity and consistency. Based on these observations, the 4% concentration was identified as the most reliable condition for stable suspended printing.

As shown in Figure 3(F), the variation in strand thickness at different nozzle speeds was then assessed. At a nozzle speed of 1 mm/s, the strand thickness exceeded the nozzle diameter (21 G, 0.51 mm) in both orientations. However, as nozzle speed increased, strand thickness decreased steadily, ultimately dropping below the nozzle diameter. Among all tested speeds, a nozzle speed of 2 mm/s produced the most consistent and accurate strand thickness, closely matching the nozzle diameter in both vertical (dPCL: 0.51 ± 0.08 mm; dPCL/HA: 0.55 ± 0.02 mm) and horizontal (dPCL: 0.46 ± 0.11 mm; dPCL/HA: 0.50 ± 0.02 mm) orientations as presented in Figure 3(G) and (H). Accordingly, 2 mm/s was determined to be the optimal printing speed for achieving uniform extrusion with minimal thickness deviation.

Subsequently, the strand thickness error was assessed in both vertical and horizontal orientations, as shown in Figure 3(I). The strand thickness errors also varied by orientation, with vertical strands showing lower error than horizontal ones, indicating superior control and stability in the vertical direction. Compared to dPCL alone, the dPCL/HA composite showed a 70% enhancement in printability in the vertical direction and an 85% enhancement in the horizontal direction. This improvement is attributed to the presence of HA particles, which act as physical reinforcements within the bioink. These particles help maintain printed shape fidelity by reducing spreading and deformation following extrusion, thereby increasing consistency in line thickness and improving overall printing accuracy [23,38,39].

This study also investigated the axial position error, a key parameter in 3D printing. This improvement effectively reduced thickness errors in both vertical and horizontal orientations.

However, the first ten layers exhibited increased deposition errors, with positional error values reaching approximately 20 to 25% (Figure 3(K)). This phenomenon is attributed to the unique environment of suspended 3D printing, where the nozzle is positioned within the support medium [12,15]. During this phase, gaps temporarily form and are subsequently refilled as the support medium recovers. During initial layer deposition, the nozzle displaces the previously recovered support medium surrounding the printed strands, which significantly reduces the accuracy of initial deposition. In contrast to conventional 3D printing methods, suspended 3D printing necessitates a narrower vertical printing step size to achieve stable layering, which contributes to increased positional errors in the initial layers. Beyond the tenth layer, the positional error significantly decreased and stabilized at a value below 1%. This stabilization likely stemmed from the support medium and nozzle reaching equilibrium, mitigating the effects of temporary pressure differences [15,40]. Both dPCL and dPCL/HA inks presented nearly identical outcomes, with no significant differences in positional error (Figure 3(I)). The observed stabilization is crucial for achieving reliable and precise structures in suspended 3D printing, particularly for ensuring consistent accuracy in subsequent layers. These findings underscore the robustness and reliability of the printing process.

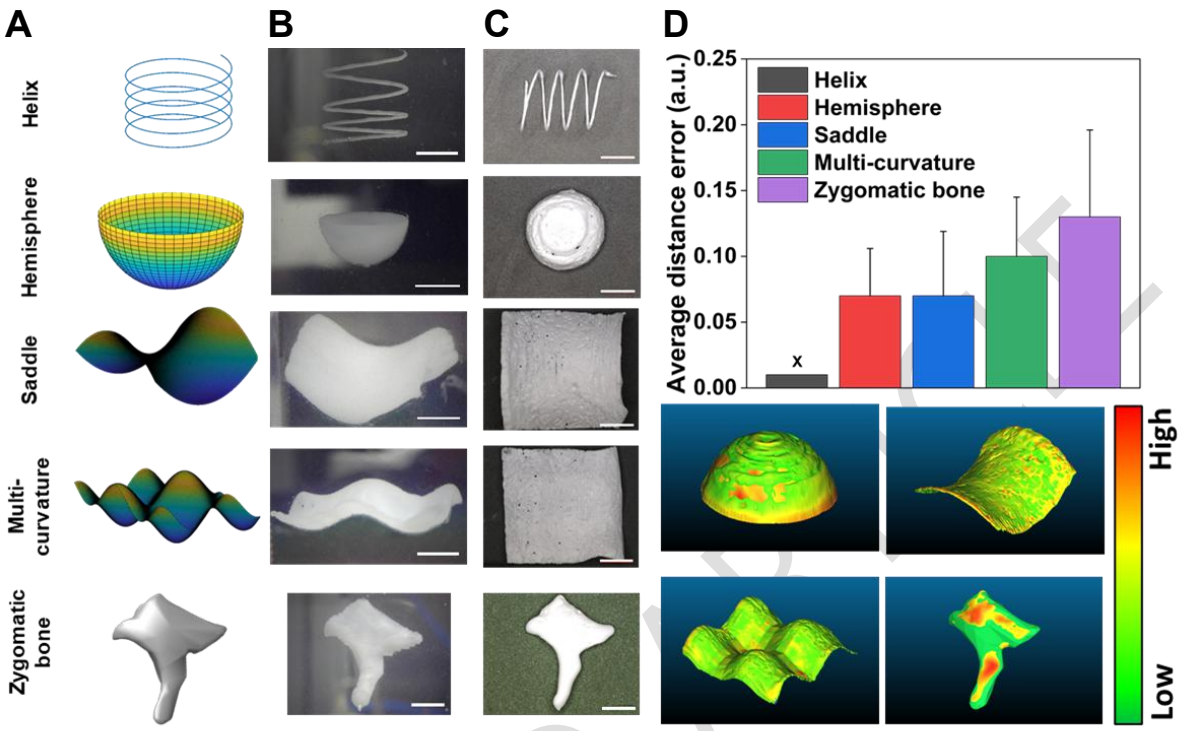

Figure 4. Suspended 3D printing of complex structures, including a helix, saddle, multi-curvature, hemisphere, and zygomatic bone. (A) Structure designs, (B) suspended 3D-printed structures within the support medium, and (C) the structures after washing the support medium. (D) Structures comparing the designed models with the printed structures. (Scale bar = 5 mm)

Based on these results, suspended 3D printing offered a significant advantage in fabricating intricate, unsupported geometries that are challenging for conventional extrusion-based methods. As exemplified by the helical structure in Figure 4, this technique enabled the creation of continuous, linear curved forms [41]. However, conventional extrusion techniques inherently struggled to fabricate complex geometries without relying on additional support structures [42,43]. The hemisphere, saddle, and multi-curvature structures further demonstrated the distinct capabilities of suspended 3D printing for fabricating complex geometries without the need for internal infill or support structures. The hemisphere confirmed the feasibility of producing hollow forms in both horizontal and vertical orientations, thereby enhancing material efficiency and reduced processing time. Concurrently, the saddle and multi-curvature structures—defined by continuous topographical variation—extended the applicability of suspended printing to

geometries with higher structural complexity than flat planes [44,45]. This capability to reliably deposit materials on surfaces with varying curvature radii highlights the potential of suspended 3D printing for freeform shape fabrication.

A more advanced and practical structure was fabricated to further demonstrate the feasibility of this method compared to conventional extrusion-based techniques. A natural zygomatic bone was selected for fabrication using the suspended 3D printing method, as its continuous curvature variations and multi-layered configurations pose technical challenges for support-free printing approaches [46-49]. The zygomatic bone is a critical component of the facial skeleton, playing an essential role in maintaining facial structure and protecting the ocular region. However, its complex curved surface architecture renders it particularly vulnerable to deformation caused by gravity when fabricated using conventional extrusion-based 3D printing techniques [47,49,50]. As demonstrated in Figure 4(D), structural comparisons were executed using a 3D optical profiler. The printed zygomatic bone was vertically scanned, and deviations from the reference model were subsequently analyzed. The geometric discrepancies were quantified using CloudCompare software and represented through a color map, in which red indicated larger deviations and green exhibited smaller errors. The findings confirmed uniform printing precision across a wide range of geometries, with minimal substantial deviations. A comparative analysis between the designed STL model and the scanned suspended structure revealed that increasing geometric complexity led to a gradual increase in average distance error, reaching over 0.1 [51,52]. As demonstrated in Figure 5, the structures fabricated using the suspended 3D printing method exhibited superior and more consistent print quality in all four directions (front, back, left, and right) compared to those produced by conventional FDM techniques [8,9,53].

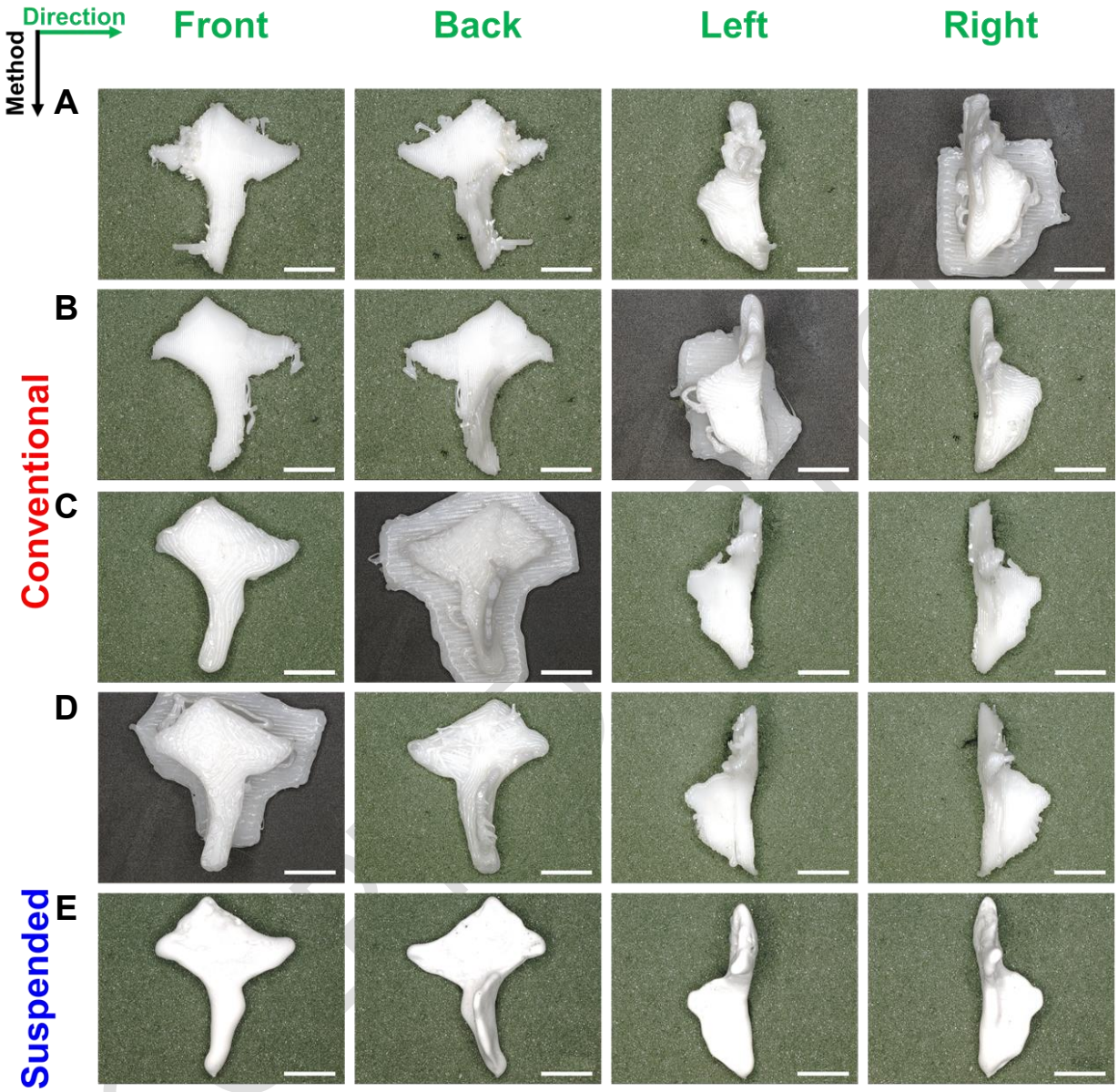

Figure 5. Comparison of zygomatic bone structures fabricated by suspended and conventional extrusion-based 3D printing. Images of the structure using the conventional method printed in (A) rightward, (B) leftward, (C) backward, and (D) forward directions. (E) Images of the structure fabricated using suspended 3D printing. Images organized by front, back, left, and right views. (Scale bar = 5 mm)

In the last step of this research, mechanical and biological properties of the scaffolds were experimentally investigated. As depicted in Figure 6(B-E), the compressive moduli were measured for dPCL/HA (105.06 ± 24.87 MPa), dPCL (58.22 ± 0.73 MPa), and PCL (136.83 ± 22.37 MPa). Among all materials, dPCL had the lowest compressive modulus. This lower modulus can be attributed to the morphology, as observed in the structural analysis, which showed higher porosity, potentially leading to a reduction in mechanical properties (see Figure 2(C-F)). The compressive stress-strain curve of dPCL/HA exhibited a significant increase after 20% strain, reflecting enhanced resistance to deformation under compressive loads. Also, dPCL showed a steady increase but with lower compressive strength compared to dPCL/HA. The enhancement in compressive modulus corresponds with the conversion of porous regions within the scaffold into denser, non-porous structures. The generation of microscale voids during solvent evaporation was found to compromise the structural integrity of the material. While dPCL exhibited superior tensile strength, its compressive strength was reduced due to the presence of voids. Conversely, in the dPCL/HA composite, HA particles embedded within the dPCL matrix served as structural reinforcements, effectively compensating for this limitation. This enhanced mechanical support suggests that dPCL/HA is more suitable than dPCL alone for load-bearing bone applications [26]. Consequently, the addition of HA enhanced the compressive properties, consistent with previous studies that highlighted the beneficial effects of HA in composite materials [20,22,54].

In the tensile test, the tensile moduli were reported as dPCL/HA (116.10 ± 9.39 MPa), dPCL (178.37 ± 47.86 MPa), and PCL (394.05 ± 36.35 MPa). Contrary to the compressive test, dPCL showed higher tensile strength than dPCL/HA. All three bioinks exhibited a significant increase in stress up to 20% strain, but their trends diverged thereafter depending on the material. For PCL, stress decreased after 20% strain until approximately 50%, after which it stabilized. However, both dPCL/HA and dPCL maintained a stable profile beyond 20% strain. Furthermore, dPCL/HA and dPCL demonstrated lower tensile performance overall, with dPCL/HA exhibiting even lower values than dPCL. This reduction is attributed to the presence of HA interfering with the intermolecular bonding of PCL, consistent with previous studies [1,54]. Notably, the mechanical

properties of dPCL/HA fall within the range of the compressive properties of cancellous bone, suggesting its potential suitability for applications in load-bearing bone scaffolds [55,56].

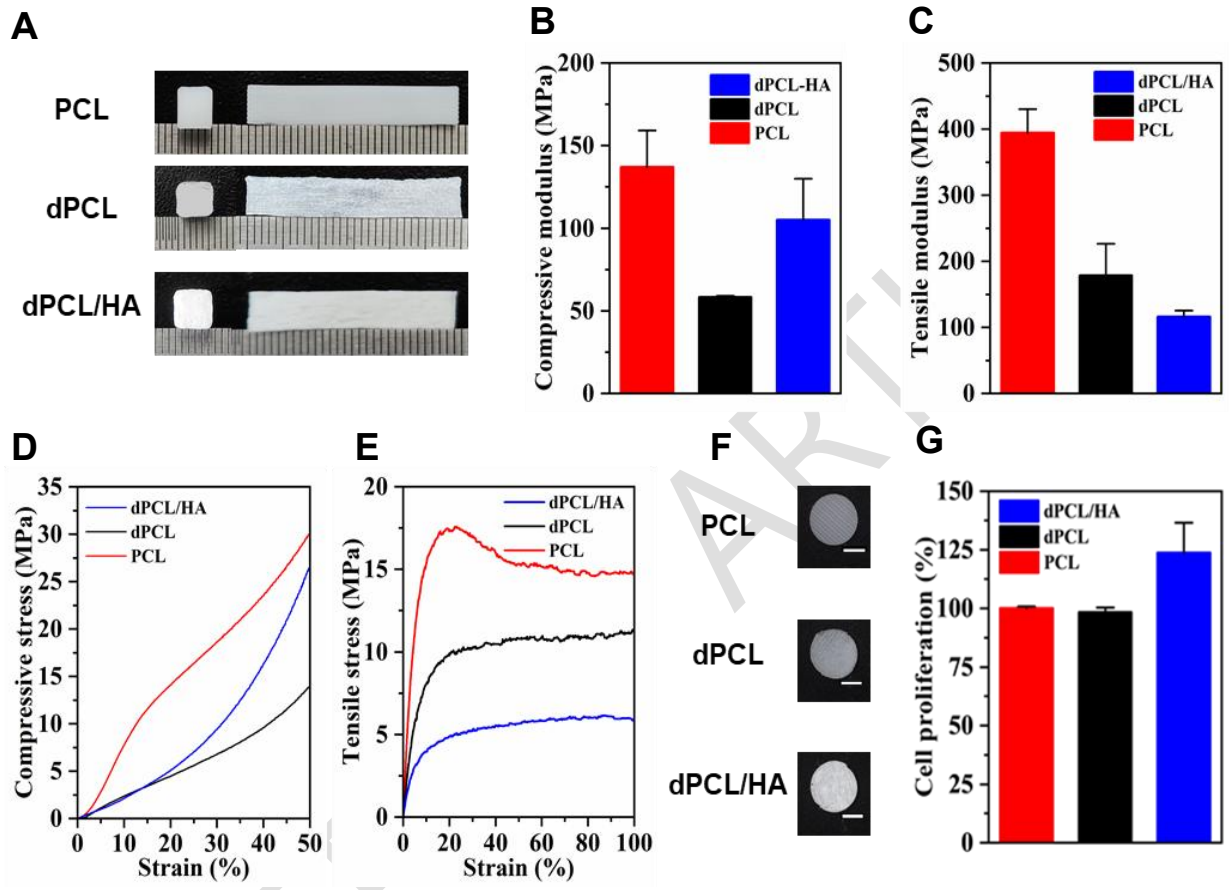

Figure 6. (A) Fabricated specimens for the mechanical assessment. (B) Compressive and (C) tensile modulus of PCL, dPCL, and dPCL/HA. (D) Compressive and (E) tensile stress-strain curves of scaffolds. (F) Specimens of the biological analysis (scale bar = 2 mm), and (G) cell proliferation tests of rADSCs on various scaffolds.

The cell proliferation of rADSCs on both PCL and PCL-based composite scaffolds was assessed using the alamarBlue assay (Figure 6(G)). The results showed comparable cell proliferation for PCL (100%) and dPCL (98.28%), while dPCL/HA (123.72%) exhibited higher cell proliferation than control (PCL) and dPCL. The comparative analysis yielded equivalent biocompatibility for the rADSCs cultured on both PCL and dPCL scaffolds, implying that dPCL did not detrimentally impact cellular toxicity after fabrication. However, no significant difference in cell proliferation

was observed between PCL and dPCL, despite their morphological differences [30,57]. In contrast, dPCL/HA demonstrated a marked improvement in cell proliferation, surpassing that of both PCL and dPCL. This enhancement suggests a pivotal role of HA in promoting biocompatibility, supported by both the morphological characteristics observed in this study and previous findings [26].These results highlight the potential of dPCL/HA scaffolds for improved cell compatibility in bone tissue engineering applications.

4. Conclusion

In summary, dPCL/HA scaffolds were systematically evaluated using suspended 3D printing to assess both material and structural performance. To fabricate precisely controlled scaffolds, a comprehensive printability assessment was conducted to optimize the various printing parameters. The incorporation of HA into dPCL significantly enhanced printability, improving resolution by up to 85% in the horizontal direction compared to pure dPCL. This advancement enabled the fabrication of complex geometries without the need for additional support structures. In addition, the dPCL/HA scaffolds showed improved mechanical performance, with compressive strengths approximately 50 MPa higher than dPCL alone. In contrast to conventional printing methods, the proposed support-free suspended printing strategy demonstrated the capability to produce structurally intricate constructs. These findings suggest the developed room-temperature, dissolved-PCL-based suspended printing approach holds significant promise for fabricating geometrically complex and biocompatible scaffolds in bone tissue engineering applications.

Acknowledgments

Not applicable.

Funding

This research was supported by a National Research Foundation of Korea (NRF) grant (NRF-2021R1I1A3040459) funded by the Korean government (MOE). This research was supported by a grant of the Korea Health Technology R&D Project through the Korea Health Industry Development Institute (KHIDI), funded by the Ministry of Health & Welfare, Republic of Korea (grant number: HI22C1323).

Conflict of interest

Seung Yun Nam serves as the Editorial Board Member of the journal, but did not in any way involve in the editorial and peer-review process conducted for this paper, directly or indirectly. Other authors declare they have no competing interests

Author contributions

Conceptualization: Juhyun Kang, Masoud Shirzad, Seung Yun Nam
Data curation: Juhyun Kang, Masoud Shirzad
Formal analysis: Juhyun kang
Funding acquisition: Seung Yun Nam
Investigation: Juhyun Kang, Masoud Shirzad, Mahdi Bodaghi, Sudip Mondal, Hae Gyun Lim, Junghwan Oh
Methodology: Juhyun Kang, Masoud Shirzad, Priya Ranganathan, Dageon Oh, Sudip Mondal
Project administration: Seung Yun Nam
Resource: Seung Yun Nam
Software: Juhyun Kang

Supervision: Seung Yun Nam
Validation: Juhyun Kang
Visualization: Juhyun Kang, Masoud Shirzad
Writing – original draft: Juhyun Kang, Masoud Shirzad
Writing – review & editing: Juhyun Kang, Masoud Shirzad, Priya Ranganathan, Dageon Oh, Sudip Mondal, Junghwan Oh, Hae Gyun Lim, Mahdi Bodaghi, Seung Yun Nam

Ethics approval and consent to participate

Not applicable.

Consent for publication

Not applicable.

Availability of data

The data that support the findings of this study are available from the corresponding author upon reasonable request.

References

[1] Deng X, Yu C, Zhang X, et al. A chitosan-coated PCL/nano-hydroxyapatite aerogel integrated with a nanofiber membrane for providing antibacterial activity and guiding bone regeneration. *Nanoscale*. May 23 2024;16(20):9861-9874. doi:10.1039/d4nr00563e

[2] Song T, Zhou J, Shi M, et al. Osteon-mimetic 3D nanofibrous scaffold enhances stem cell proliferation and osteogenic differentiation for bone regeneration. *Biomater Sci*. Feb 15 2022;10(4):1090-1103. doi:10.1039/d1bm01489g

[3] Romanazzo S, Molley TG, Nemec S, et al. Synthetic Bone-Like Structures Through Omnidirectional Ceramic Bioprinting in Cell Suspensions. *Advanced Functional Materials*. 2021;31(13)doi:10.1002/adfm.202008216

[4] Kim MH, Chalisserry EP, Mondal S, Oh J, Nam SY. Silicon-substituted hydroxyapatite reinforced 3D printed gelatin membrane for guided bone regeneration. *Materials Letters*. 2021;304doi:10.1016/j.matlet.2021.130670

[5] Lee H, Yoo JM, Ponnusamy NK, Nam SY. 3D-printed hydroxyapatite/gelatin bone scaffolds reinforced with graphene oxide: Optimized fabrication and mechanical characterization. *Ceramics International*. 2022;48(7):10155-10163.

[6] Montalbano G, Molino G, Fiorilli S, Vitale-Brovarone C. Synthesis and incorporation of rod-like nano-hydroxyapatite into type I collagen matrix: A hybrid formulation for 3D printing of bone scaffolds. *Journal of the European Ceramic Society*. 2020;40(11):3689-3697. doi:10.1016/j.jeurceramsoc.2020.02.018

[7] Shirzad M, Kang J, Kim G, Bodaghi M, Nam SY. Bioinspired 3D-Printed Auxetic Structures with Enhanced Fatigue Behavior. *Advanced Engineering Materials*. 2024;doi:10.1002/adem.202302036

[8] Hu K, Jin S, Wang CC. Support slimming for single material based additive manufacturing. *Computer-Aided Design*. 2015;65:1-10.

[9] Jiang J, Xu X, Stringer J. Support structures for additive manufacturing: a review. *Journal of Manufacturing and Materials Processing*. 2018;2(4):64.

[10] Alioglu MA, Yilmaz YO, Singh YP, et al. Nested Biofabrication: Matryoshka-Inspired Intra-Embedded Bioprinting. *Small Methods*. Dec 19 2023:e2301325. doi:10.1002/smtd.202301325

[11] Song KH, Highley CB, Rouff A, Burdick JA. Complex 3D-Printed Microchannels within Cell-Degradable Hydrogels. *Advanced Functional Materials*. 2018;28(31)doi:10.1002/adfm.201801331

[12] Bhattacharjee T, Zehnder SM, Rowe KG, et al. Writing in the granular gel medium. *Science advances*. 2015;1(8):e1500655.

[13] Wu W, DeConinck A, Lewis JA. Omnidirectional printing of 3D microvascular networks. *Adv Mater*. Jun 24 2011;23(24):H178-83. doi:10.1002/adma.201004625

[14] Jin Y, Compaan A, Chai W, Huang Y. Functional Nanoclay Suspension for Printing-Then-Solidification of Liquid Materials. *ACS Appl Mater Interfaces*. Jun 14 2017;9(23):20057-20066. doi:10.1021/acsami.7b02398

[15] Lee A, Hudson A, Shiwarski D, et al. 3D bioprinting of collagen to rebuild components of the human heart. *Science*. 2019;365(6452):482-487.

[16] Gao C, Sow WT, Wang Y, et al. Hydrogel composite scaffolds with an attenuated immunogenicity component for bone tissue engineering applications. *J Mater Chem B*. Mar 4 2021;9(8):2033-2041. doi:10.1039/d0tb02588g

[17] Liu L, Yang B, Wang LQ, et al. Biomimetic bone tissue engineering hydrogel scaffolds constructed using ordered CNTs and HA induce the proliferation and differentiation of BMSCs. *J Mater Chem B*. Jan 22 2020;8(3):558-567. doi:10.1039/c9tb01804b

[18] Mondal S, Dey A, Pal U. Low temperature wet-chemical synthesis of spherical hydroxyapatite nanoparticles and their in situ cytotoxicity study. *Advances in nano research*. 2016;4(4):295-307. doi:10.12989/anr.2016.4.4.295

[19] Shi Y, Wang L, Sun L, et al. Melt electrospinning writing PCL scaffolds after alkaline modification with outstanding cytocompatibility and osteoinduction. *International Journal of Bioprinting*. 2023;9(6)doi:10.36922/ijb.1071

[20] Biscaia S, Branquinho MV, Alvites RD, et al. 3D Printed Poly(ε-caprolactone)/Hydroxyapatite Scaffolds for Bone Tissue Engineering: A Comparative Study on a Composite Preparation by Melt Blending or Solvent Casting Techniques and the Influence

of Bioceramic Content on Scaffold Properties. *Int J Mol Sci*. Feb 19 2022;23(4)doi:10.3390/ijms23042318

[21] Rezaei A, Mohammadi MR. Development of hydroxyapatite nanorods-polycaprolactone composites and scaffolds derived from a novel in-situ sol-gel process. *Tissue Engineering and Regenerative Medicine*. 2012;9(6):295-303. doi:10.1007/s13770-012-0002-z

[22] Wang Y, Liu L, Guo S. Characterization of biodegradable and cytocompatible nano-hydroxyapatite/polycaprolactone porous scaffolds in degradation in vitro. *Polymer Degradation and Stability*. 2010;95(2):207-213.

[23] Cestari F, Petretta M, Yang Y, Motta A, Grigolo B, Sglavo VM. 3D printing of PCL/nano-hydroxyapatite scaffolds derived from biogenic sources for bone tissue engineering. *Sustainable Materials and Technologies*. 2021;29doi:10.1016/j.susmat.2021.e00318

[24] Zeng X, Meng Z, Qiu Z, He J, Fan J, Li D. Melt-based embedded printing for freeform fabrication of overhanging and flexible polycaprolactone scaffolds. *Virtual and Physical Prototyping*. 2023;18(1)doi:10.1080/17452759.2023.2209778

[25] Jakus AE, Rutz AL, Jordan SW, et al. Hyperelastic "bone": A highly versatile, growth factor–free, osteoregenerative, scalable, and surgically friendly biomaterial. *Science translational medicine*. 2016;8(358):358ra127-358ra127.

[26] Moghadam MZ, Hassanajili S, Esmaeilzadeh F, Ayatollahi M, Ahmadi M. Formation of porous HPCL/LPCL/HA scaffolds with supercritical CO2 gas foaming method. *Journal of the mechanical behavior of biomedical materials*. 2017;69:115-127.

[27] Lee H-U, Jeong Y-S, Jeong S-Y, et al. Role of reactive gas in atmospheric plasma for cell attachment and proliferation on biocompatible poly ε-caprolactone film. *Applied Surface Science*. 2008;254(18):5700-5705.

[28] Liu Z, Liu X, Ramakrishna S. Surface engineering of biomaterials in orthopedic and dental implants: Strategies to improve osteointegration, bacteriostatic and bactericidal activities. *Biotechnology journal*. 2021;16(7):2000116.

[29] Wang L, Wang C, Zhou L, et al. Fabrication of a novel Three-Dimensional porous PCL/PLA tissue engineering scaffold with high connectivity for endothelial cell migration. *European Polymer Journal*. 2021;161doi:10.1016/j.eurpolymj.2021.110834

[30] Ma J, Lin L, Zuo Y, et al. Modification of 3D printed PCL scaffolds by PVAc and HA to enhance cytocompatibility and osteogenesis. *RSC Adv*. Feb 11 2019;9(10):5338-5346. doi:10.1039/c8ra06652c

[31] Oh D, Shirzad M, Chang Kim M, Chung E-J, Nam SY. Rheology-informed hierarchical machine learning model for the prediction of printing resolution in extrusion-based bioprinting. *International Journal of Bioprinting*. 2023;9(6)doi:10.36922/ijb.1280

[32] Kim MH, Lee YW, Jung WK, Oh J, Nam SY. Enhanced rheological behaviors of alginate hydrogels with carrageenan for extrusion-based bioprinting. *J Mech Behav Biomed Mater*. Oct 2019;98:187-194. doi:10.1016/j.jmbbm.2019.06.014

[33] Huang B, Bártolo PJ. Rheological characterization of polymer/ceramic blends for 3D printing of bone scaffolds. *Polymer Testing*. 2018;68:365-378.

[34] He M, Zhang F, Li C, et al. Mechanical properties and oral restoration applications of 3D printed aliphatic polyester-calcium composite materials. *Alexandria Engineering Journal*. 2024;88:245-252. doi:10.1016/j.aej.2024.01.042

[35] Motloung MP, Mofokeng TG, Ray SS. Viscoelastic, Thermal, and Mechanical Properties of Melt-Processed Poly (epsilon-Caprolactone) (PCL)/Hydroxyapatite (HAP) Composites. *Materials (Basel)*. Dec 24 2021;15(1)doi:10.3390/ma15010104

[36] Daskalakis E, Hassan MH, Omar AM, Cooper G, Weightman A, Bartolo P. Rheological behaviour of different composite materials for additive manufacturing of 3D bone scaffolds. *journal of materials research and technology*. 2023;24:3670-3682.

[37] Waters R, Alam P, Pacelli S, Chakravarti AR, Ahmed RP, Paul A. Stem cell-inspired secretome-rich injectable hydrogel to repair injured cardiac tissue. *Acta biomaterialia*. 2018;69:95-106.

[38] Guo C, Wu J, Zeng Y, Li H. Construction of 3D bioprinting of HAP/collagen scaffold in gelation bath for bone tissue engineering. *Regenerative Biomaterials*. 2023;10:rbad067.

[39] Milazzo M, Fitzpatrick V, Owens CE, et al. 3D printability of silk/hydroxyapatite composites for microprosthetic applications. *ACS Biomaterials Science & Engineering*. 2023;9(3):1285-1295.

[40] Hinton TJ, Jallerat Q, Palchesko RN, et al. Three-dimensional printing of complex biological structures by freeform reversible embedding of suspended hydrogels. *Science advances*. 2015;1(9):e1500758.

[41] Wu Q, Zhu F, Wu Z, et al. Suspension printing of liquid metal in yield-stress fluid for resilient 3D constructs with electromagnetic functions. *npj Flexible Electronics*. 2022;6(1):50.

[42] Enea S, Moon SK. Guidelines for 3D printed springs using material extrusion. *Rapid Prototyping Journal*. 2022;28(3):409-427.

[43] Okutani C, Yokota T, Miyazako H, Someya T. 3D Printed Spring-Type Electronics with Liquid Metals for Highly Stretchable Conductors and Inductive Strain/Pressure Sensors. *Advanced Materials Technologies*. 2022;7(7):2101657.

[44] Rodriguez-Padilla C, Cuan-Urquizo E, Roman-Flores A, Gordillo JL, Vázquez-Hurtado C. Algorithm for the conformal 3D printing on non-planar tessellated surfaces: Applicability in patterns and lattices. *Applied Sciences*. 2021;11(16):7509.

[45] Abdullah AM, Dunn ML, Yu K. Robotic 3D printing of continuous fiber reinforced thermoset composites. *Advanced Materials Technologies*. 2024;9(24):2400839.

[46] Murali A, Parameswaran R. Extrusion 3D printing advances for craniomaxillofacial bone tissue engineering. *Polymer-Plastics Technology and Materials*. 2024;63(7):889-912.

[47] Tao O, Kort-Mascort J, Lin Y, et al. The applications of 3D printing for craniofacial tissue engineering. *Micromachines*. 2019;10(7):480.

[48] Meglioli M, Naveau A, Macaluso GM, Catros S. 3D printed bone models in oral and cranio-maxillofacial surgery: a systematic review. *3D printing in medicine*. 2020;6:1-19.

[49] Nyberg E, O'Sullivan A, Grayson W. scafSLICR: A MATLAB-based slicing algorithm to enable 3D-printing of tissue engineering scaffolds with heterogeneous porous microarchitecture. *PloS one*. 2019;14(11):e0225007.

[50] Moiduddin K, Mian SH, Umer U, Alkhalefah H, Ahmed F, Hashmi FH. Design, analysis, and 3D printing of a patient-specific polyetheretherketone implant for the reconstruction of zygomatic deformities. *Polymers*. 2023;15(4):886.

[51] Van Belleghem S, Torres Jr L, Santoro M, et al. Hybrid 3D printing of synthetic and cell-laden bioinks for shape retaining soft tissue grafts. *Advanced functional materials*. 2020;30(3):1907145.

[52] Shiwarski DJ, Hudson AR, Tashman JW, et al. 3D bioprinting of collagen-based high-resolution internally perfusable scaffolds for engineering fully biologic tissue systems. *Science Advances*. 2025;11(17):eadu5905.

[53] Guerrero-de-Mier A, Espinosa M, Domínguez M. Bricking: A new slicing method to reduce warping. *Procedia Engineering*. 2015;132:126-131.

[54] Moeini S, Mohammadi MR, Simchi A. In-situ solvothermal processing of polycaprolactone/hydroxyapatite nanocomposites with enhanced mechanical and biological performance for bone tissue engineering. *Bioact Mater*. Sep 2017;2(3):146-155. doi:10.1016/j.bioactmat.2017.04.004

[55] Shirzad M, Bodaghi M, Oh D, Yi M, Nam SY. Design and optimization of bioinspired auxetic structure for biomedical applications. *European Journal of Mechanics - A/Solids*. 2024;103doi:10.1016/j.euromechsol.2023.105139

[56] Almela T, Brook IM, Khoshroo K, et al. Simulation of cortico-cancellous bone structure by 3D printing of bilayer calcium phosphate-based scaffolds. *Bioprinting*. 2017;6:1-7. doi:10.1016/j.bprint.2017.04.001

[57] Huang B, Caetano G, Vyas C, Blaker JJ, Diver C, Bartolo P. Polymer-Ceramic Composite Scaffolds: The Effect of Hydroxyapatite and beta-tri-Calcium Phosphate. *Materials (Basel)*. Jan 14 2018;11(1)doi:10.3390/ma11010129